Supporting Information

Effect of solvents on multifunctional Dy_2 complexes with axial chiral ligands (*R*)/(*S*)-1,1′-binaphthyl-2,2′-diyl phosphate

Cai-Ming Liu,*[,a] Yi-Quan Zhang,*[,b] Xiang Hao,[a] and Xi-Li Li[c]

[a] *Beijing National Laboratory for Molecular Sciences, CAS Key Laboratory for Organic Solids, Center for Molecular Science, Institute of Chemistry, Chinese Academy of Sciences, Beijing 100190, China.*

[b] *Ministry of Education Key Laboratory of NSLSCS, School of Physical Science and Technology, Nanjing Normal University, Nanjing 210023, China.*

[c] *Henan Provincial Key Laboratory of Surface and Interface Science, Zhengzhou University of Light Industry, Zhengzhou 450002, China*

Contents

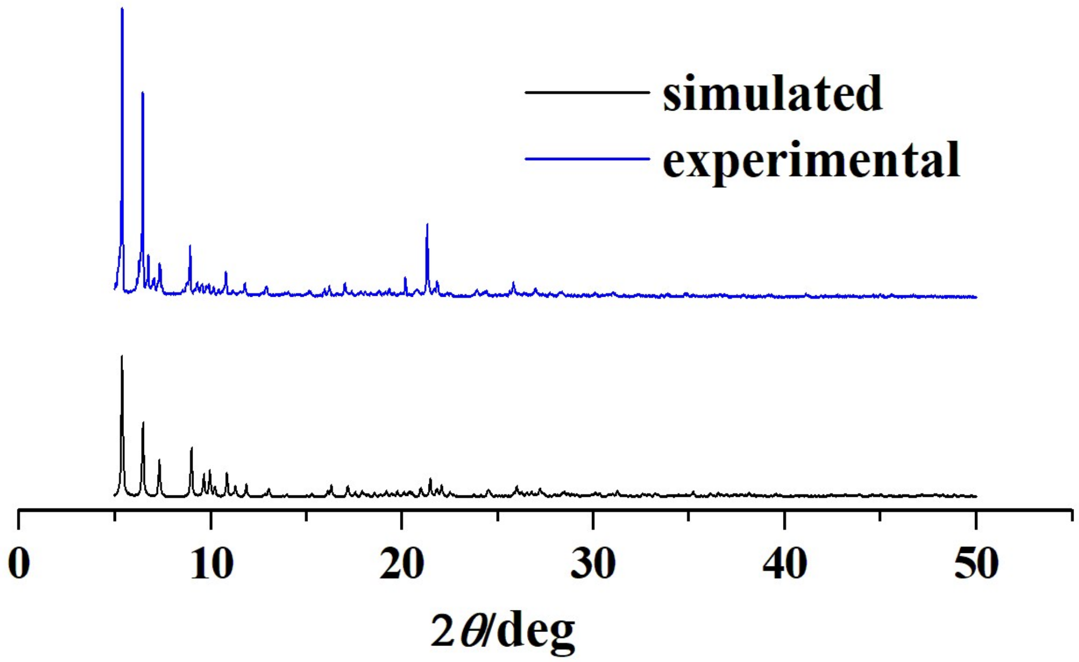

Fig. S1. The simulative and experimental powder X-ray diffraction patterns for *R*-**1**.

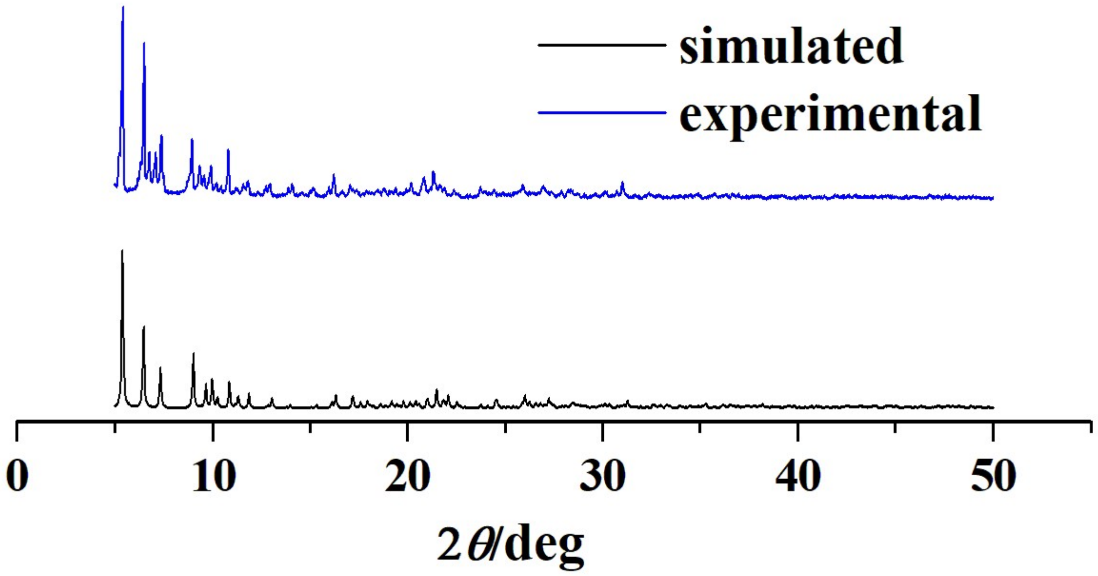

Fig. S2. The simulative and experimental powder X-ray diffraction patterns for *S*-**1**.

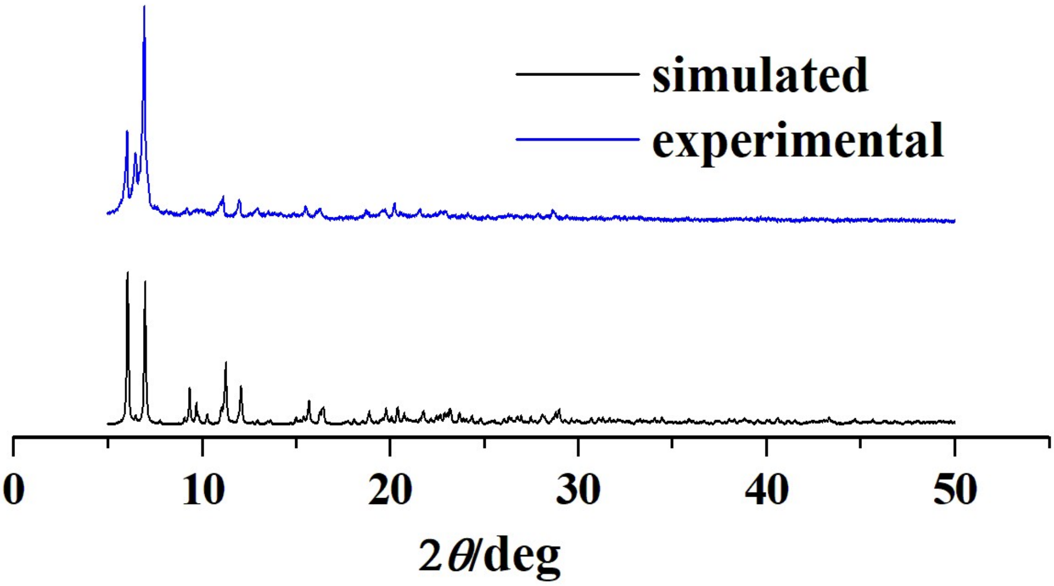

Fig. S3. The simulative and experimental powder X-ray diffraction patterns for *R*-**2**.

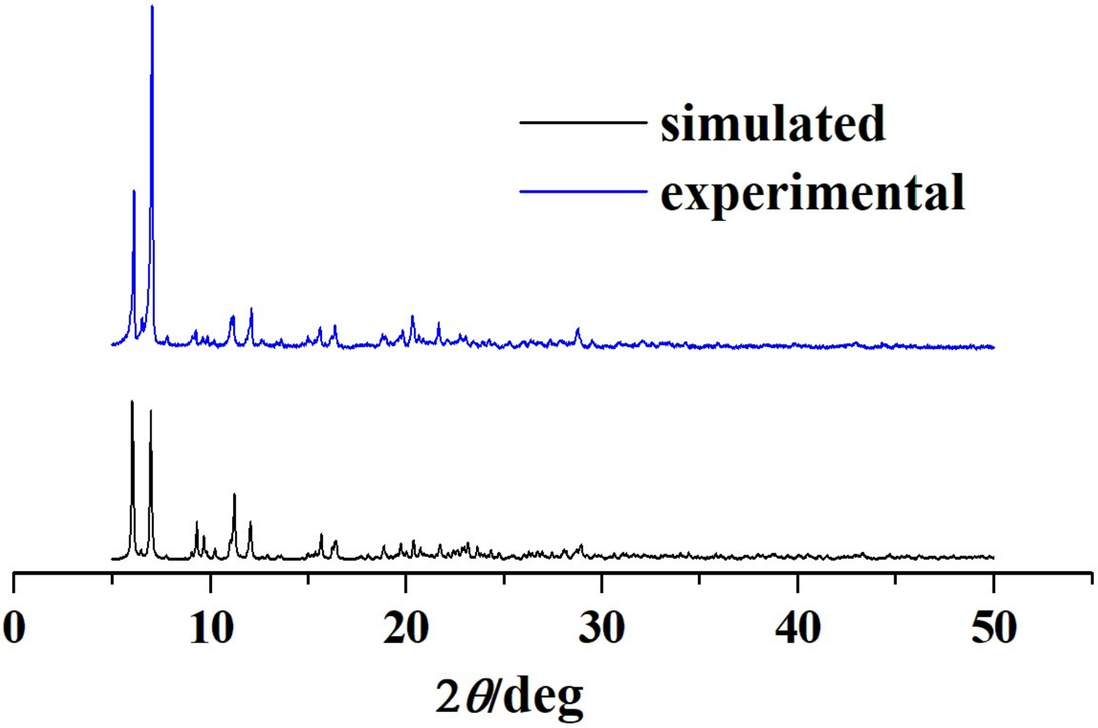

Fig. S4. The simulative and experimental powder X-ray diffraction patterns for *S*-**2**.

Table S1. Selected bond lengths (Å) and angles (°) of *R*-**1** and *R*-**2**.

R-**1**			
Dy(1)-N(1)	2.470(9)	Dy(1)-N(6)	2.554(10)
Dy(1)-O(1)	2.194(8)	Dy(1)-O(2)	2.385(8)
Dy(1)-O(4)	2.346(7)	Dy(1)-O(5)	2.374(8)
Dy(1)-O(9)	2.373(7)	Dy(1)-O(13)	2.373(9)
Dy(2)-N(3)	2.558(9)	Dy(2)-N(4)	2.477(9)
Dy(2)-O(2)	2.373(8)	Dy(2)-O(3)	2.220(8)
Dy(2)-O(4)	2.411(8)	Dy(2)-O(6)	2.352(8)
Dy(2)-O(10)	2.333(7)	Dy(2)-O(14)	2.385(8)
O(4)-Dy(1)-O(2)	69.5(2)	O(2)-Dy(2)-O(4)	68.6(2)
O(4)-Dy(1)-N(6)	66.2(3)	O(1)-Dy(1)-N(1)	73.5(3)
O(2)-Dy(1)-N(1)	64.6(3)	O(9)-Dy(1)-O(5)	145.8(3)
O(2)-Dy(2)-N(3)	63.8(3)	O(3)-Dy(2)-N(4)	72.3(3)
O(4)-Dy(2)-N(4)	63.5(3)	O(10)-Dy(2)-O(6)	144.8(3)
R-**2**			
Dy(1)-N(1)	2.479(10)	Dy(1)-N(6)	2.508(10)
Dy(1)-O(1)	2.218(8)	Dy(1)-O(2)	2.364(9)
Dy(1)-O(4)	2.387(8)	Dy(1)-O(5)	2.350(7)
Dy(1)-O(9)	2.340(8)	Dy(1)-O(13)	2.410(8)
Dy(2)-N(3)	2.581(10)	Dy(2)-N(4)	2.525(10)
Dy(2)-O(2)	2.391(8)	Dy(2)-O(3)	2.215(8)
Dy(2)-O(4)	2.396(8)	Dy(2)-O(6)	2.303(8)
Dy(2)-O(10)	2.363(7)	Dy(2)-O(14)	2.402(9)
O(2)-Dy(1)-O(4)	68.9(3)	O(2)-Dy(2)-O(4)	68.3(3)
O(4)-Dy(1)-N(6)	65.7(3)	O(1)-Dy(1)-N(1)	74.1(3)
O(2)-Dy(1)-N(1)	63.9(3)	O(9)-Dy(1)-O(5)	142.9(3)
O(3)-Dy(2)-N(4)	73.3(3)	O(4)-Dy(2)-N(4)	62.5(3)
O(2)-Dy(2)-N(3)	64.5(3)	O(6)-Dy(2)-O(10)	147.7(3)

Table S2. Dy (III) ion geometry analysis by SHAPE 2.1 software for *R*-**1**.

Configuration	ABOXIY **Dy1**	ABOXIY **Dy2**
Octagon(D_{8h})	32.854	32.834
Heptagonal pyramid(C_{7v})	22.251	21.825
Hexagonal bipyramid(D_{6h})	12.117	11.524
Cube (O_h)	7.629	7.264
Square antiprism (D_{4d})	3.029	2.331
Triangular dodecahedron (D_{2d})	**1.143**	**2.011**
Johnson gyrobifastigium J26 (D_{2d})	12.922	12.381
Johnson elongated triangular bipyramid J14 (D_{3h})	26.057	26.144
Biaugmented trigonal prism J50 (C_{2v})	3.468	3.696
Biaugmented trigonal prism (C_{2v})	2.942	2.711
Snub diphenoid J84 (D_{2d})	4.368	5.524
Triakis tetrahedron (T_d)	8.465	8.123
Elongated trigonal bipyramid (D_{3h})	22.519	23.161

Table S3. Dy (III) ion geometry analysis by SHAPE 2.1 software for *R*-**2**.

Configuration	ABOXIY **Dy1**	ABOXIY **Dy2**
Octagon(D_{8h})	32.831	33.066
Heptagonal pyramid(C_{7v})	21.678	21.587
Hexagonal bipyramid(D_{6h})	12.333	10.470
Cube (O_h)	8.187	7.037
Square antiprism (D_{4d})	2.154	2.632
Triangular dodecahedron (D_{2d})	**2.081**	**2.392**
Johnson gyrobifastigium J26 (D_{2d})	12.748	11.574
Johnson elongated triangular bipyramid J14 (D_{3h})	28.490	25.265
Biaugmented trigonal prism J50 (C_{2v})	3.234	4.141
Biaugmented trigonal prism (C_{2v})	2.128	3.090
Snub diphenoid J84 (D_{2d})	5.451	6.263
Triakis tetrahedron (T_d)	8.886	7.749
Elongated trigonal bipyramid (D_{3h})	23.549	22.716

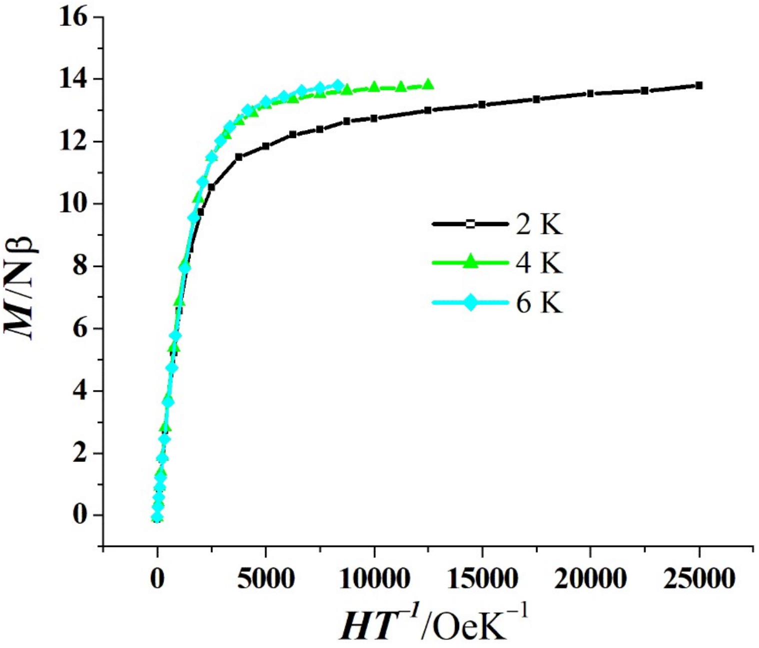

Fig. S5. *M versus H*/*T* plots at 2,4 and 6 K of *R*-**1**.

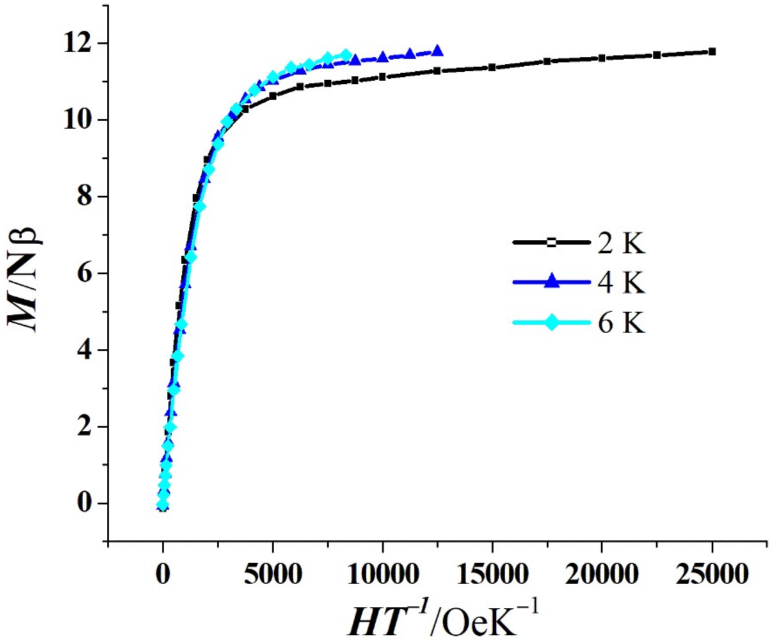

Fig. S6. *M versus H*/*T* plots at 2, 4 and 6 K of *R*-**2**.

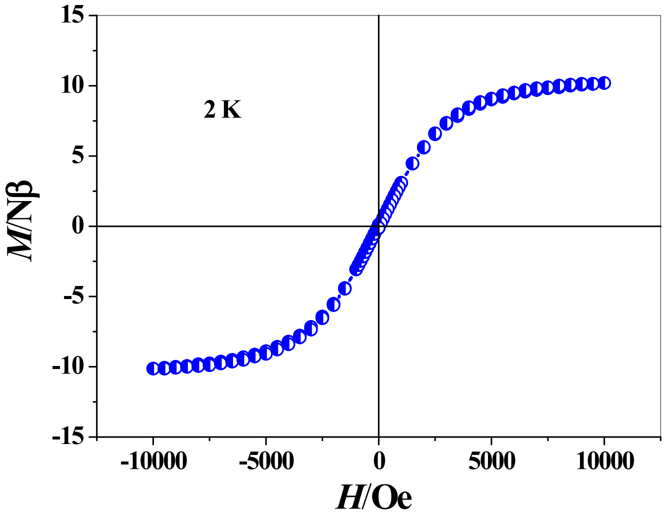

Fig. S7. Hysteresis loop for *R*-**1** at 2 K.

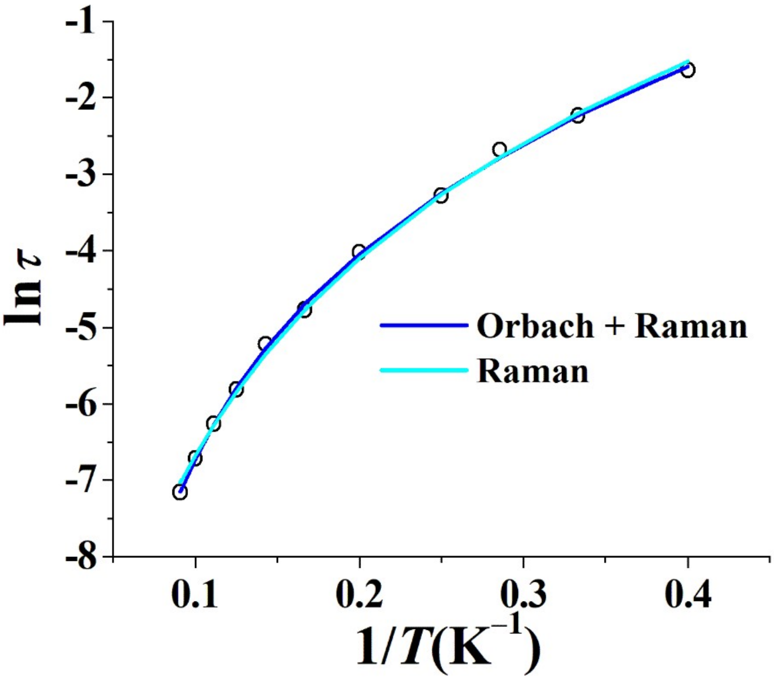

Fig. S8. Plot of lnτ *versus* $1/T$ for *R*-**1** (H_{dc} = 1500 Oe), the solid line represents the best fitting with Orbach + Raman or Raman only.

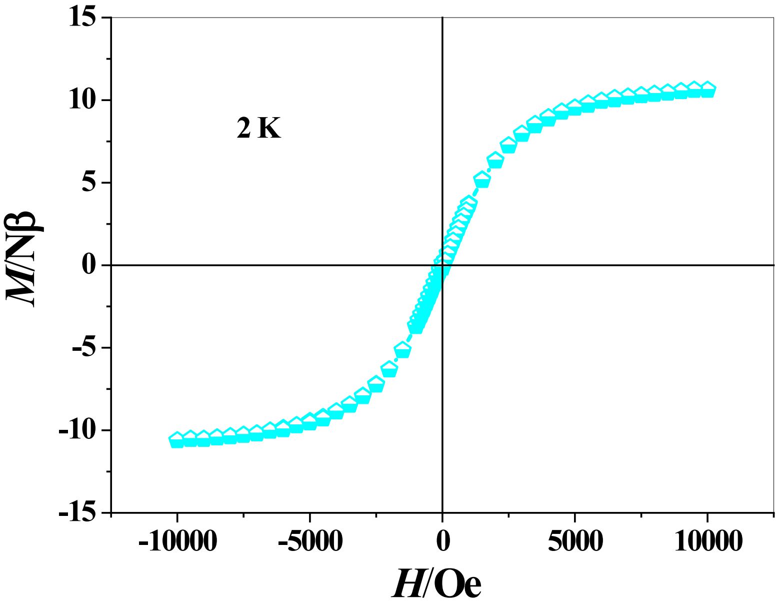

Fig. S9. Hysteresis loop for *R*-**2** at 2 K.

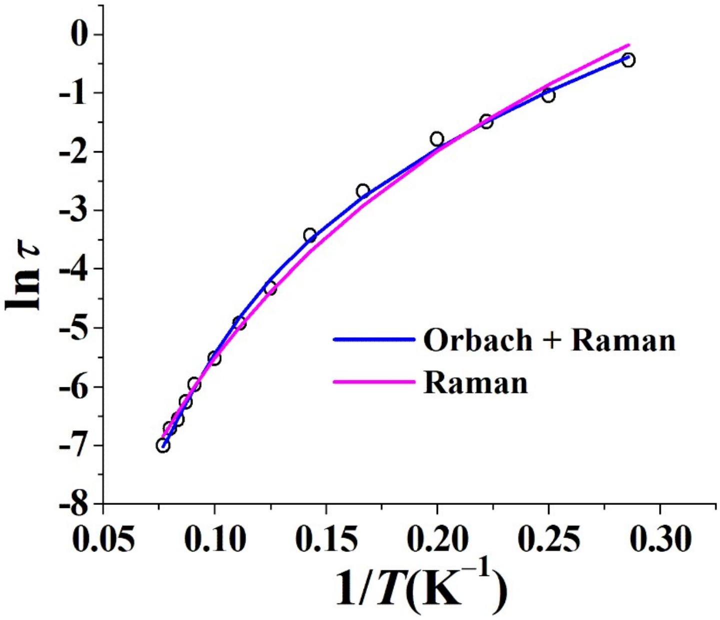

Fig. S10. Plot of lnτ *versus* 1/T for *R*-**2** (H_{dc} = 1500 Oe), the solid line represents the best fitting with Orbach + Raman or Raman only.

Computational details

Considering the non-centrosymmetric structures of the binuclear complexes *R*-**1** and *R*-**2**, we need to calculate two types of individual Dy^{III} fragments for each of them. Complete-active-space self-consistent field (CASSCF) calculations on individual Dy^{III} fragments for complexes *R*-**1** and *R*-**2** (see Figure S11 for the calculated structures of them) on the basis of single-crystal X-ray determined geometry have been carried out with the OpenMolcas[S1] program package. Each individual Dy^{III} fragment was calculated keeping the experimentally determined structure of the corresponding compound while replacing the neighboring Dy^{III} ion by diamagnetic Lu^{III}.

The basis sets for all atoms are atomic natural orbitals from the OpenMolcas[S1] ANO-RCC library: ANO-RCC-VTZP for Dy^{III}; VTZ for close N and O; VDZ for distant atoms. The calculations employed the second order Douglas-Kroll-Hess Hamiltonian, where scalar relativistic contractions were taken into account in the basis set and the spin-orbit couplings were handled separately in the restricted active space state interaction (RASSI-SO) procedure.[S2–S3] Active electrons in 7 active orbitals include all *f* electrons (CAS (9 in 7) in the CASSCF calculation. To exclude all the doubts, we calculated all the roots in the active space. We have mixed the maximum number of spin-free state which was possible with our hardware (all from 21 sextets, 128 from 224 quadruplets, 130 from 490 doublets for Dy^{III}. SINGLE_ANISO[S4–S6] program was used to obtain the energy levels, ***g*** tensors, magnetic axes, *et al.* based on the above CASSCF/RASSI-SO calculations.

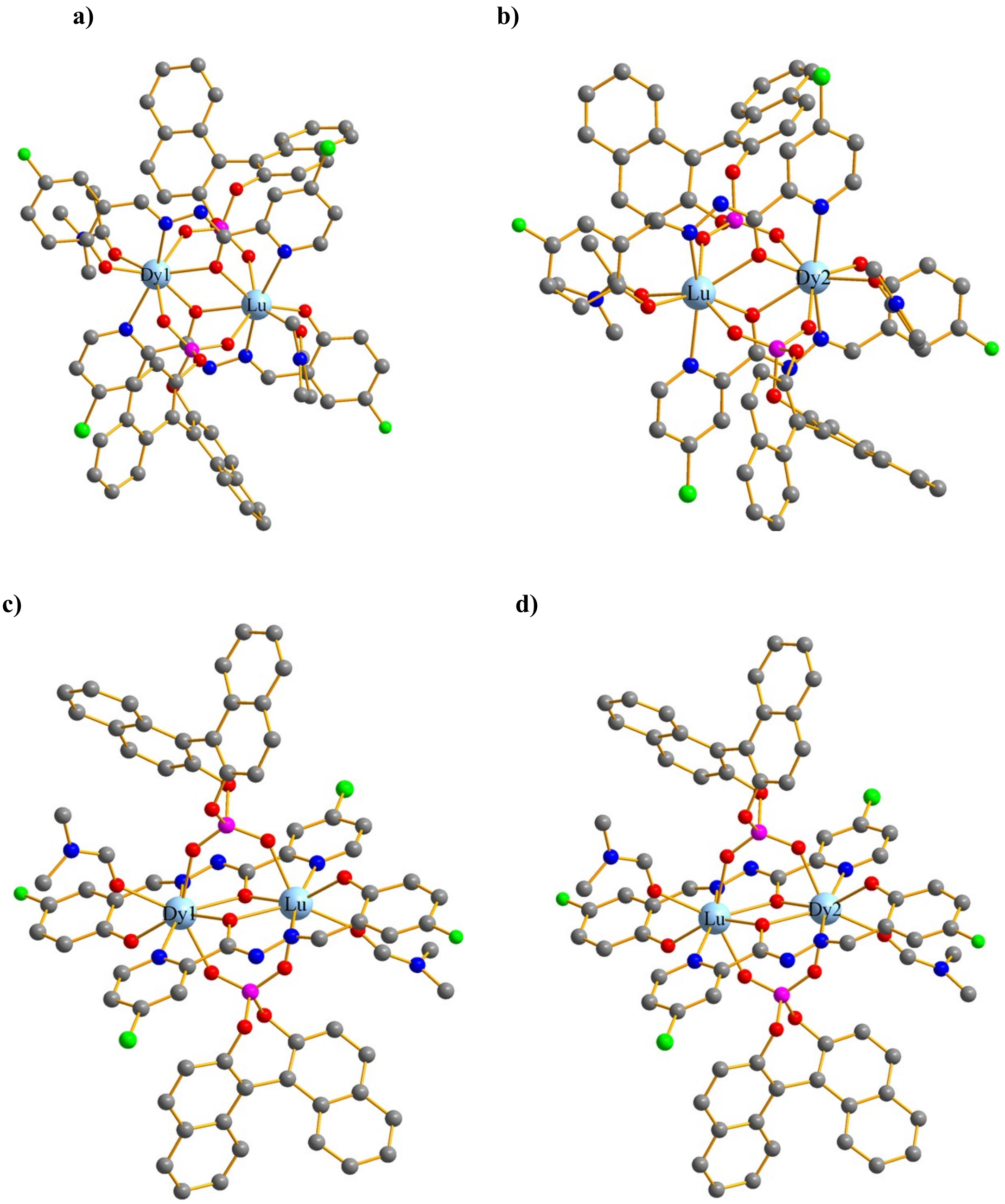

Fig. S11. Calculated individual Dy^{III} fragments of *R*-**1**_Dy1 (a), *R*-**1**_Dy2 (b), *R*-**2**_Dy1 (c) and *R*-**2**_Dy2 (d); H atoms are omitted for clarify.

Table S4. Calculated energy levels (cm^{-1}), ***g*** (g_x, g_y, g_z) tensors and predominant m_J values of the lowest eight Kramers doublets (KDs) of individual Dy^{III} fragments for *R*-**1** and *R*-**2** using CASSCF/RASSI-SO with the OpenMolcas.

KDs	*R*-**1**_Dy1			*R*-**1**_Dy2		
	E	***g***	m_J	*E*	***g***	m_J
0	0.0	0.022 0.022 19.675	±15/2	0.0	0.021 0.0295 19.690	±15/2
1	151.7	0.109 0.128 16.790	±13/2	158.3	0.219 0.291 16.803	±13/2
2	296.3	2.167 2.676 12.480	±11/2	295.7	2.468 3.949 11.802	
3	358.5	0.164 2.835 12.669		373.2	8.107 6.762 1.114	
4	303.1	8.457 6.736 2.216		447.0	0.661 2.902 14.017	
5	383.0	2.180 5.870 10.820		488.4	1.181 3.404 12.674	
6	429.6	1.741 2.670 15.457		534.7	1.130 2.220 13.394	
7	530.5	1.301 3.305 14.617		567.2	0.221 0.846 16.092	
KDs	*R*-**2**_Dy1			*R*-**2**_Dy2		
	E	***g***	m_J	*E*	***g***	m_J
0	0.0	0.043 0.064 19.615	±15/2	0.0	0.017 0.025 19.684	±15/2

1	152.3	0.421 0.631 16.426	±13/2	150.8	0.203 0.251 16.704	±13/2
2	256.5	3.752 5.654 10.342		278.3	1.390 1.707 13.013	
3	306.8	0.528 2.999 12.982		364.5	1.551 4.592 9.493	
4	346.4	1.652 3.676 13.239		427.3	1.072 2.506 14.380	
5	432.9	0.060 2.026 14.353		461.0	2.842 3.766 11.370	
6	500.1	0.936 1.891 13.370		534.7	1.103 2.394 13.075	
7	524.3	0.764 2.756 16.029		569.1	0.777 3.498 15.503	

Table S5. Wave functions with definite projection of the total moment | m_J > for the lowest eight KDs of individual Dy^{III} fragments for *R*-**1** and *R*-**2**.

	E/cm^{-1}	wave functions
R-**1**_Dy1	0.0	97.4%|±15/2>
	151.7	93.2%|±13/2>
	296.3	79.2%|±11/2>+6.6%|±5/2>+6.3%|±3/2>
	358.5	36.2%|±1/2>+22.7%|±3/2>+17.9%|±9/2>+13.5%|±5/2>
	303.1	28.3%|±9/2>+23.3%|±3/2>+21.0%|±7/2>+15.7%|±5/2>+6.9%|±1/2>
	383.0	35.2%|±1/2>+21.7%|±9/2>+16.7%|±7/2>+13.0%|±5/2>+11.1%|±3/2>
	429.6	25.8%|±7/2>+24.1%|±3/2>+19.0%|±9/2>+14.8%|±5/2>+11.4%|±1/2>
	530.5	34.9%|±5/2>+26.7%|±7/2>+12.3%|±3/2>+9.7%|±9/2>+8.1%|±11/2>
R-**1**_Dy2	0.0	97.8%|±15/2>
	158.3	91.5%|±13/2>
	295.7	67.8%|±11/2>+9.6%|±3/2>+5.8%|±5/2>+4.5%|±7/2>+3.8%|±9/2>
	373.2	30.7%|±9/2>+24.9%|±1/2>+14.5%|±3/2>+11.2%|±5/2>+11.0%|±11/2>
	447.0	24.0%|±1/2>+22.7%|±3/2>+18.4%|±9/2>+15.7%|±5/2>+11.8%|±7/2>
	488.4	30.3%|±9/2>+28.4%|±7/2>+15.2%|±5/2>+14.1%|±3/2>+6.3%|±11/2>
	534.7	33.7%|±1/2>+33.1%|±7/2>+13.1%|±5/2>+8.9%|±3/2>+7.9%|±9/2>
	567.2	37.0%|±5/2>+30.0%|±3/2>+13.6%|±7/2>+7.3%|±9/2>+6.1%|±1/2>
R-**2**_Dy1	0.0	96.9%|±15/2>
	152.3	88.7%|±13/2>+4.9%|±5/2>
	256.5	56.8%|±11/2>+18.0%|±3/2>+9.1%|±1/2>+6.9%|±9/2>
	306.8	29.0%|±1/2>+19.8%|±5/2>+14.4%|±9/2>+14.1%|±3/2>+10.1%|±11/2>+9.5%|±7/2>
	346.4	34.2%|±9/2>+16.2%|±7/2>+15.2%|±11/2>+13%|±3/2>+10.4%|±3/2>7.8%|±5/2>
	432.9	29.6%|±7/2>+25.7%|±9/2>+15.7%|±5/2>+15.2%|±3/2>+5.8%|±11/2>
	500.1	31.8%|±7/2>+28.7%|±5/2>+17.6%|±1/2>+9.6%|±9/2>+5.2%|±11/2>
	524.3	37.9%|±3/2>+25.4%|±1/2>+19.9%|±5/2>+7.6%|±9/2>
R-**1**_Dy2	0.0	97.8%|±15/2>
	150.8	91.4%|±13/2>
	278.3	72.6%|±11/2>+8.4%|±5/2>+6.4%|±7/2>+6.2%|±3/2>
	364.5	39.5%|±9/2>+17.0%|±3/2>+15.9%|±1/2>+9.7%|±5/2>+9.2%|±11/2>
	427.3	26.5%|±1/2>+19.4%|±3/2>+18.4%|±9/2>+16.6%|±5/2>+14.6%|±7/2>
	461.0	26.9%|±7/2>+22.2%|±9/2>+17.6%|±1/2>+13.9%|±5/2>+13.1%|±3/2>
	534.7	32.7%|±1/2>+32.5%|±7/2>+14.3%|±3/2>+11.0%|±5/2>
	569.1	38.5%|±5/2>+29.9%|±3/2>+10.4%|±7/2>+8.0%|±9/2>+6.8%|±11/2>

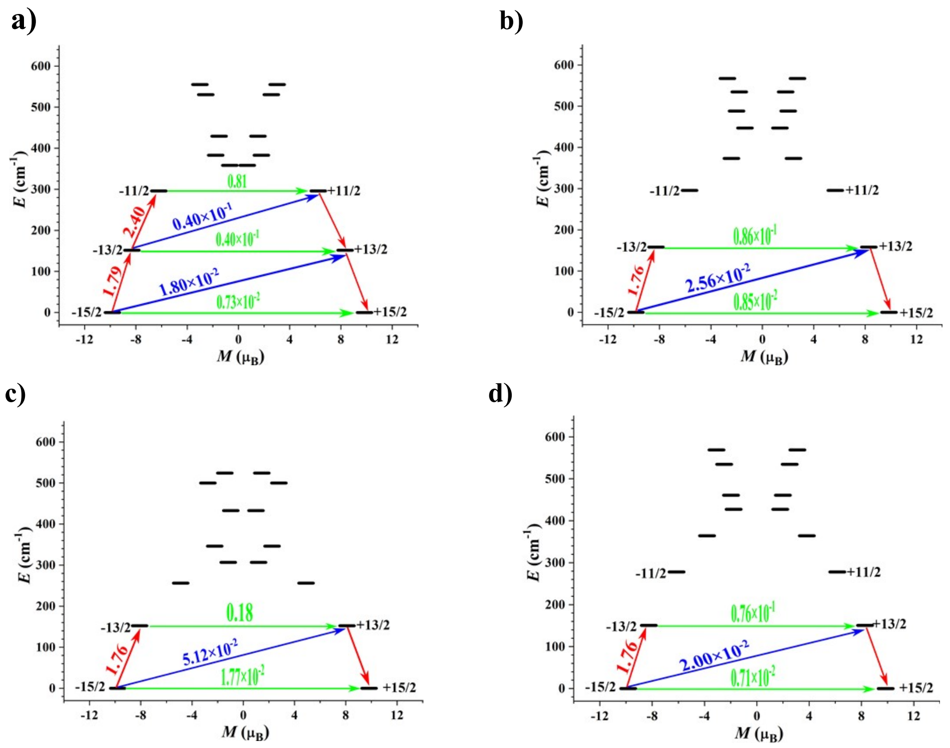

Fig. S12. Magnetization blocking barriers of individual Dy^{III} fragments of *R*-**1**_Dy1 (a), *R*-**1**_Dy2 (b), *R*-**2**_Dy1 (c) and *R*-**2**_Dy2 (d). The thick black lines represent the KDs as a function of their magnetic moment along the magnetic axis. The green lines correspond to diagonal quantum tunneling of magnetization (QTM); the blue line represent off-diagonal relaxation process. The numbers at each arrow stand for the mean absolute value of the corresponding matrix element of transition magnetic moment.

To fit the exchange interactions in complexes *R*-**1** and *R*-**2**, we took two steps to obtain them. Firstly, we calculated individual Dy^{III} fragments using CASSCF/RASSI-SO to obtain the corresponding magnetic properties. Then, the exchange interaction between the magnetic centers was considered within the Lines model,[S7] while the account of the dipole-dipole magnetic coupling was treated exactly. The Lines model is effective and has been successfully used widely in the research field of *d* and *f*-elements single-molecule magnets.[S8-S9]

For each of complexes *R*-**1** and *R*-**2**, there is only one type of $\tilde{J}$. The Ising exchange Hamiltonian is:

$$\hat{H}_{exch} = -\tilde{J}\hat{\tilde{S}}_{Dy1}\hat{\tilde{S}}_{Dy2} \tag{S1}$$

$\tilde{J} = 25\cos\varphi J$, where φ is the angle between the anisotropy axes on two Dy^{III} sites, and *J* is the Lines exchange coupling parameter. $\tilde{S}_{Dy} = 1/2$ is the ground pseudospin on the Dy^{III} site. $\tilde{J}_{total}$ is the effective parameter of the total magnetic interaction ($\tilde{J}_{total} = \tilde{J}_{dip} + \tilde{J}_{exch}$) between magnetic center ions. The dipolar magnetic coupling can be calculated exactly, while the exchange coupling constant was fitted through comparison of the computed and measured magnetic susceptibilities using the POLY_ANISO program.[S4–S6]

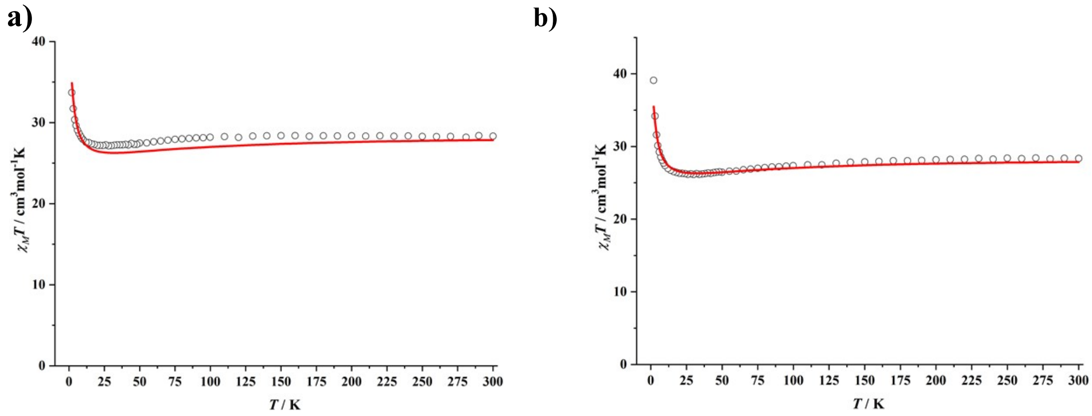

Fig. S13. Calculated (red solid line) and experimental (black square dot) data of magnetic susceptibilities of *R*-**1** (a) and *R*-**2** (b). The intermolecular interactions *zJ′* of complexes *R*-**1** and *R*-**2** were both fitted to –0.01 cm^{-1}.

Table S6. Exchange energies *E* (cm^{-1}), the energy difference between each exchange doublets Δ_t (cm^{-1}) and the main values of the g_z for the lowest two exchange doublets of *R*-**1** and *R*-**2**.

	R-**1**			*R*-**2**		
	E	Δ_t	g_z	*E*	Δ_t	g_z
1	0.000000000000	0.123×10^{-5}	39.328	0.000000000000	0.270×10^{-5}	39.277
	0.000001229075			0.000002701564		
2	2.101619694314	0.374×10^{-5}	1.719	2.286129110575	0.483×10^{-5}	1.314
	2.101623438914			2.286133939751		

References:

S1 I. F. Galván, M. Vacher, A. Alavi, C. Angeli, F. Aquilante, J. Autschbach, J. J. Bao, S. I. Bokarev, N. A. Bogdanov, R. K. Carlson, L. F. Chibotaru, J. Creutzberg, N. Dattani, M. G. Delcey, S. S. Dong, A. Dreuw, L. Freitag, L. M. Frutos, L. Gagliardi, F. Gendron, A. Giussani, L. González, G. Grell, M. Y. Guo, C. E. Hoyer, M. Johansson, S. Keller, S. Knecht, G. Kovacevic, E. Källman, G. L. Manni, M. Lundberg, Y. J. Ma, S. Mai, J. P. Malhado, P. Å. Malmqvist, P. Marquetand, S. A. Mewes, J. Norell, M. Olivucci, M. Oppel, Q. M. Phung, K. Pierloot, F. Plasser, M. Reiher, A. M. Sand, I. Schapiro, P. Sharma, C. J. Stein, L. K. Sørensen, D. G. Truhlar, M. Ugandi, L. Ungur, A. Valentini, S. Vancoillie, V. Veryazov, O. Weser, T. A. Wesołowski, Per-Olof.

Widmark, S. Wouters, A. Zech, J. P. Zobel and R. Lindh, OpenMolcas: From Source Code to Insight. *J. Chem. Theory Comput.*, 2019, **15**, 5925-5964.

S2 P. Å. Malmqvist, B. O. Roos and B. Schimmelpfennig, *Chem. Phys. Lett.,* 2002, **357***,* 230-240.

S3 B. A. Heß, C. M. Marian, U. Wahlgren and O. Gropen, *Chem. Phys. Lett.,* 1996, **251***,* 365-371.

S4 L. F. Chibotaru, L. Ungur and A. Soncini, *Angew. Chem., Int. Ed.*, 2008, **47**, 4126-4129.

S5 L. Ungur, W. Van den Heuvel and L. F. Chibotaru, *New J. Chem.*, 2009, **33**, 1224-1230.

S6 L. F. Chibotaru, L. Ungur, C. Aronica, H. Elmoll, G. Pilet and D. Luneau, *J. Am. Chem. Soc*. **2008**, *130*, 12445-12455.

S7 M. E. Lines, *J. Chem. Phys*., 1971, **55**, 2977-2984.

S8 K. C. Mondal, A. Sundt, Y. H. Lan, G. E. Kostakis, O. Waldmann, L. Ungur, L. F. Chibotaru, C. E. Anson and A. K. Powell, *Angew. Chem., Int. Ed.*, 2012, **51**, 7550-7554.

S9 S. K. Langley, D. P. Wielechowski, V. Vieru, N. F. Chilton, B. Moubaraki, B. F. Abrahams, L. F. Chibotaru and K. S. Murray, *Angew. Chem., Int. Ed.,* 2013, **52**, 12014-12019.

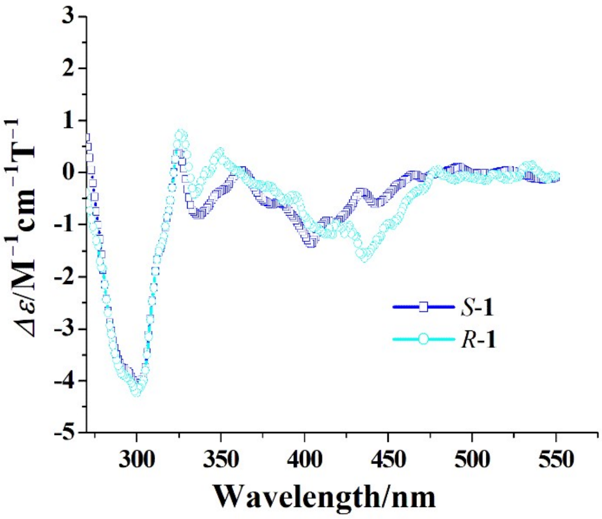

Fig. S14. MCD spectra of *R*-**1** and *S*-**1**.

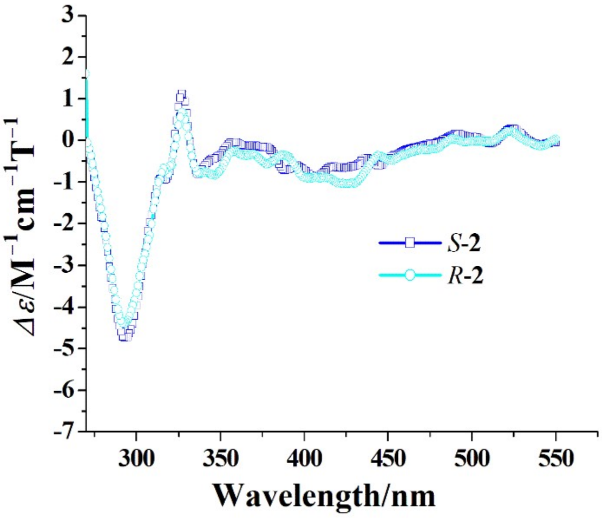

Fig. S15. MCD spectra of *R*-**2** and *S*-**2**.